NASA-CR-205335

SOOT VOLUME FRACTION IMAGING

Paul S. Greenberg
NASA-Lewis Research Center
Cleveland, OH 44135

Jerry. C. Ku
Mechanical Engineering Department
Wayne State University
Detroit, MI 48202

ABSTRACT

A new technique is described for the full-field determination of soot volume fractions via laser extinction measurements. This technique differs from previously reported point-wise methods in that a two-dimensional array (i.e. image) of data is acquired simultaneously. In this fashion, the net data rate is increased, allowing the study of time-dependent phenomena and the investigation of spatial and temporal correlations. A telecentric imaging configuration is employed to provide depth-invariant magnification and to permit the specification of the collection angle for scattered light. To improve the threshold measurement sensitivity, a method is employed to suppress undesirable coherent imaging effects. A discussion of the tomographic inversion process is provided, including the results obtained from numerical simulations. Results obtained with this method from an ethylene diffusion flame are shown to be in close agreement with those previously obtained by sequential, point-wise interrogation.

Introduction

Of the various optical diagnostics for the characterization of soot volume fractions in flames, methods based on extinction have been utilized most extensively.[1-4] This is due in part to the relatively large optical cross sections, affording the measurement of small concentrations. The experimental configuration is straightforward to implement, resulting in data that is simple to analyze. Studies to date have relied on sequential point-wise interrogation of the soot field.[3-4] By translating the position of the optics relative to the flame, spatially resolved absorption data is obtained over some region of interest. This represents a time consuming process, inadequate for transient phenomena.

We have developed a technique for the simultaneous, rapid acquisition of two-dimensional extinction data. The method utilizes solid-state detector arrays coupled with collection optics configured to provide depth-invariant magnification and characterized angular collection efficiency. Undesirable coherent imaging effects and fluctuations in source stability are taken into account to improve measurement sensitivity. A system constructed from inexpensive, commercially available components has been used to determine fractional absorbances as low as 4×10^{-3} at a full-field acquisition rate of 30 Hz. The system is simple, mechanically stable, and can be configured in a compact fashion, rendering it useful for a variety of applications.

Measurement of Optical Extinction

Optical extinction can be used to determine soot volume fractions for those particles whose absorption and scattering can be approximated by Rayleigh theory. The discussion here essentially follows that of Santoro et al in their prior studies of laminar diffusion flames.[3] Neglecting multiple scattering and radiant

emission at the detection wavelength, the extinction of optical radiation, I_λ, by a quasi-continuous medium obeys the Bouguer-Lambert-Beer law.[5]

$$\frac{dI_\lambda}{ds} = -k_{e\lambda} I_\lambda \tag{1}$$

ds being the incremental path length and $k_{e\lambda}$ the optical extinction coefficient at the source wavelength. Integrating equation (1) along chord-like paths through the flame yields:

$$\ln(I_\lambda / I_{\lambda 0}) = \int_{-\infty}^{+\infty} k_{e\lambda} ds \tag{2}$$

In the Rayleigh limit ($D \ll \lambda$), the extinction coefficient is given by:

$$k_{e\lambda} = \frac{\pi^2}{\lambda} E(\tilde{m}) N \int_0^{\infty} P(D) D^3 dD \tag{3}$$

where $\tilde{m}$ is the complex refractive index of the particle, N the number of particles, and $E(\tilde{m})$ is given by:

$$E(\tilde{m}) = -\mathrm{Im}\left(\frac{\tilde{m}^2 - 1}{\tilde{m}^2 + 2}\right) \tag{4}$$

The quantity P(D)dD represents the probability of occurrence of particle diameters between D and D + dD, thus $\int P(D)\, dD$ taken over all particles is equal to unity. The generalized moment ratio D_{pq} is defined as:

$$D_{pq} = \left(\frac{\int_0^{\infty} P(D) D^p dD}{\int_0^{\infty} P(D) D^q dD} \right)^{(1/p-q)} \tag{5}$$

Using this definition, the volume fraction f_v can be expressed as:

$$f_v = \frac{\pi}{6} N D_{30}^3 \qquad (6)$$

From equations (3) - (6) it follows that:

$$f_v = \frac{\lambda k_{ai}}{6\pi E(\tilde{m})} \qquad (7)$$

For this investigation, a value of $\tilde{m} = 1.7 - 0.7i$ is assumed;[6] the exact value is debated in the literature.[2,7,8] Equations (4) and (7) demonstrate that alternative values result in the variation of f_v by a multiplicative constant.

Investigations involving both scattering and analysis via transmission electron microscopy suggest that soot aggregate structures do not satisfy the criterion of individual spheres with $D \ll \lambda$, and thus the use of Rayleigh theory requires validation.[3,9,10,11] While this departure impacts scattering, first-order theory of scattering by mass fractal aggregates[12,13] and modeling analyses[14,15,16] demonstrate that absorption is only weakly affected. Furthermore, the present optical configuration allows the precise specification of collection angle, permitting the introduction of scattering corrections if desired.

Data Filtering and Tomographic Inversion

Because optical extinction is path-integrated, a single measurement of transmittance cannot determine local values of f_v. In addition, the spatial limits over which the absorbing species participate are generally not known *a priori*, precluding the evaluation of the quantity $\int ds$. For axisymmetric flames, the direct inversion can be obtained by Abel transformation.[17] Numerous approaches to this problem have been developed; the reader is referred to the recent review article by Dasch.[18]

The present work employs the filtered backprojection method of Ramachandran and Lakshminarayanan[19] using the algorithm derived by Shepp and Logan.[20] This method has been employed in numerous applications involving absorption measurements in flames, due to the resulting accuracy and computational efficiency.[3, 21-23] Before reducing experimental data, the inversion was validated with numerically simulated backprojections, including sets which investigated the behavior of the inversion in the presence of noise sources specific to coherent imaging. The two primary noise sources are attributable to the coherent effects of speckle and diffraction in the presence of first-order refraction.

In point-wise measurements, the diameter of the detector is normally chosen to exceed that of the interrogating beam to reduce sensitivity to beam steering effects. As a result, the measurement is integrated over a large number of speckles, reducing intensity variations due to speckle fluctuations.[24] Any flame perturbs the refractive index field, causing the speckle pattern in the plane of the detector to redistribute. The speckle fields are therefore not spatially stationary for reference and data images, but appear as additive noise. This is also true for coherent diffraction effects from dust particles or localized optical defects. Similarly, beam steering causes lateral shifts in the diffraction patterns; the intensity perturbations attributable to these shifted patterns are not removed by normalization by the reference image. As discussed below, this effect can be significantly reduced by corrupting the coherence of the source.

Since the derivative-like nature of Abelian inversion accentuates the presence of high frequency noise components,[18] inversion of data with additive noise is preceded here by spatial lowpass filtering. Several filtering kernels were investigated, including linearly-weighted convolution and cubic spline smoothing. Simulated data sets were created by adding normally distributed random noise to numerically generated backprojections. In all cases, the best fit to the original absorbance data was obtained from two-

dimensional tensor product B-splines.[25] Inversion of the filtered numerical simulations confirmed the accurate retrieval of the original volume fraction distributions. Subsequently, this procedure was demonstrated to replicate volume fractions ~~from absorbance data~~ previously reported by Santoro et al for laminar ethylene diffusion flames.[3]

Optical Configuration

The optical configuration is shown in Fig. 1. The beam from a low power laser is followed by a variable neutral density filter, then spatially filtered, expanded and collimated. Following the test section are imaging bandpass and neutral density filters; these filters are selected so that no detectable signal results from luminous flame emissions. The variable neutral density filter is adjusted so that the unattenuated reference image fills the dynamic range of the detector. The receiving pupil is located at the front focal plane (i.e. Fourier plane) of the weak decollimating lens. This provides a telecentric configuration possessing depth-invariant magnification.[26] In addition, the spatially-invariant angular collection efficiency is specified by r_p/f, where r_p is the radius of the pupil and f is the focal length of the decollimator. The virtual image formed by the decollimator is re-imaged onto a monochrome CCD array using a conventional camera lens. The output of the array is sent to a video-frame digitizer; the results reported here were obtained with a bus-mounted eight-bit digitizer residing in a 486 personal computer.

[Fig.1]

It is essential that the imaging system be focused on the plane corresponding to the centroid of the first moment of the refractive index taken along the direction of the optical axis. Satisfying this condition eliminates intensity variations due to second-order spatial gradients, or shadowgraph terms,[27] which would otherwise contaminate the optical extinction measurement. For radial phase objects, this plane corresponds with the axis of symmetry. In practice, optimum focus is achieved through the use of an axisymmetric

test object. In this study, a laminar jet of highly refractive gas, freon, was located coaxially with the fuel nozzle prior to the experiment. When the imaging lens was improperly focused, a shadowgraph image of the jet was clearly visible; when correctly focused this image vanished.

It is desirable to corrupt the coherence of the laser source to diminish the effects of speckle and diffraction. As discussed, these effects are not eliminated by normalization to the reference image, and must be attenuated optically. In the present configuration, this is accomplished with a rapidly rotating glass diffuser plate. Locating this plate near the common focus of the beam expander affords the use of a small diameter diffuser, and minimally decollimates the expanded beam. In using a detector array, the divergence of the collimated beam must be equal to or less than $d_p/(M \cdot d_f)$, where d_p is the lateral dimension of a pixel, M is the overall optical magnification, and d_f is the diameter of the flame. This condition validates inversion by Abel transformation, since non-overlapping chord-like paths are required. Figures 2 and 3 depict reference images obtained with and without the use of the diffuser; fig. 3 clearly demonstrates the reduction in speckle and diffraction. In addition, the intensity of the image field is spatially more uniform, as the increased angular spectrum exiting the diffuser plate effectively overfills the secondary element of the beam expander.

[Fig. 2,3]

Results and Discussion

Imaging soot volume fraction measurements were demonstrated using a laminar diffusion flame burner similar to that previously reported by Santoro et al.[3] The fuel nozzle has an inside diameter of 10.5 mm and is surrounded by a 100 mm diameter annular coflow. The entire assembly is encased in a 405 mm long cylindrical brass chimney. Optical access is provided by two circular ports machined in the walls

of the chimney. These ports are 50 mm in diameter to coincide with the diameter of the expanded laser beam. Screens and a ceramic flow restrictor are placed at the exit of the chimney to achieve a stable flame by reducing air recirculation down the interior side walls. The fuel port and coflow annulus were supplied with ethylene (3.85 cm^3/sec) and air (713.3 cm^3/sec), respectively, to coincide with prior investigations. In experiments investigating the effect of temporal averaging, these flow rates were reduced to 2 cm^3/sec and 341.7 cm^3/sec, respectively, to provide a more fully developed soot shell at the same axial locations.

To account for fluctuations in laser intensity, each image is normalized by the average intensity in a specific reference region, here a 10 x 10 pixel area located midway between the flame and the chimney wall. Care must be exercised regarding the conditions under which the reference image is acquired. In this study, the absorption image is captured after the burner reaches steady-state temperature. Best results are obtained with a reference image also corresponding to a heated burner, thus the reference image is acquired immediately after terminating the fuel flow. The air coflow, however, is maintained to eliminate transient refractive index perturbations due to mixing induced by steep thermal gradients at the walls of the chimney. These considerations can be appreciated from the observed differences between reference images corresponding to the conditions of a cold or hot burner, or a hot burner with or without the coflow maintained. This behavior is attributed to refractive index inhomogeneities caused by small geometric imperfections in the burner and buoyant mixing that result in departures from perfect axial symmetry, and thus perturb the reference image through second order optical effects.

[Fig. 4,5]

Full-field, single-shot absorbance data and the resulting soot volume fraction map for a 3.85 cm^3/sec laminar ethylene diffusion flame are shown in Figs. 4 and 5, respectively. Figures 6 and 7 provide a comparison with transmittance data and soot volume fractions at selected axial locations previously

reported by Santoro et al. Shown in Fig. 6 is raw transmittance data, as well as the results of filtering by linearly weighted, 3 x 9 pixel convolution and smoothing by tensor B-splines. As is observed in numerical simulations, the latter provides the best fit to the original data. Slight differences in the transmittance data near the burner axis at axial locations of 30 and 40 millimeters above the nozzle tip are attributed to differences in laser wavelength and hence refractive indices, and small differences in the burner (10.5 millimeter nozzle as opposed to the original 11.1 millimeters, and stainless steel as opposed to brass).

[Fig. 6,7]

The resulting soot volume fractions shown in Fig. 7 are in good agreement with previous results, and demonstrate shot-to-shot repeatability. The slightly narrower, taller peaks in maximum volume fractions are attributed to the two-fold improvement in spatial resolution (0.1 mm) afforded by the imaging configuration. The increase in noise in the neighborhood of the burner axis is characteristic of radial inversion, which tends to propagate noise from individual backprojections radially inward.[18] A direct comparison of point-wise and imaging extinction measurements (the latter using our design) performed for a laminar ethylene diffusion flame also demonstrates close agreement between soot volume fractions obtained by the two methods.[28]

The ability to acquire time-resolved, full-field data allows the closer inspection of the effect of time averaging. For example, each datum reported in reference (3) represents an average of 100 readings taken over a 10 second interval, each reading acquired by lock-in detection operating with a time constant of 0.125 seconds. For the purposes of comparison, to obtain the equivalent of one frame of 483 x 512 pixel image data by point-wise scanning would require an acquisition time of 687 hours, or 28.6 days. In the present work, temporal averages are computed for 2^n image fields, for n ranging in value from 1 to 7. For a data acquisition rate of 30 frames per second, a 128 frame average corresponds to an integration

time of 4.27 seconds.

Figure 8 shows ~~percent~~ smoothed absorbance at five axial locations for temporal averages taken over 1, 32, 64, and 128 frame averages. Noticeable differences in absorbance levels are observed, while the overall flame shape is preserved. The results suggest that the changes are due to flame movement, because the absorbance level increases at some locations, but decreases at others. Because there is no observable direction of convergence as the averaging time is increased, we however do not feel that temporal averaging will necessarily provide more meaningful data. Rather, we note that these low-Reynolds-number flames are ~~somewhat unstable, even after precaution is taken to isolate the flame from its surroundings.~~ fairly susceptible to changes in the ambient environment.

[Fig. 8]

If the difference between the smoothed and original N-point absorbance profiles at a specific axial location is used as an indication of the noise level in the original profiles, it is seen that the 128-frame image-averaged profiles are considerably less noisy than the single-shot profiles. The RMS noise, N_{RMS}, for a temporal average of 2n individual measurements is defined by:

$$N_{RMS} = \left(\frac{1}{N} \sum_{i=1}^{2^n} (A_{o,i} - A_{s,i})^2 \right)^{1/2} \qquad (8)$$

where A denotes absorbance, and the subscripts o and s denote the original and smoothed profiles, respectively. N_{RMS} varies from a maximum value of 1.25 (single-shot profile at an axial height of 10 millimeters), to a minimum value of 0.316 (128 frame-averaged profile at an axial height of 40 millimeters). Furthermore, it is observed that minimal reduction in N_{RMS} occurs beyond a value of n = 6. For the same axial locations, Fig. 9 shows both unsmoothed and smoothed profiles of single-shot and 128 frame-averaged data. The agreement between smoothed profiles leads to the conclusion that smoothed single-shot data sets provide a reasonable representation of the actual soot volume fractions.

[Fig. 9]

To account for corrections due to in-scattering, receiving pupils of different diameters were utilized, corresponding to collection angles of 0.1, 0.25, and 0.5 degrees. Under these changes, no appreciable differences were observed, a result that is consistent with Rayleigh theory and the relatively course 8-bit digitization scheme employed. Departures from this behavior become difficult to measure in practice, since the enhanced forward-scattering resulting from the increased size of aggregate structures is balanced by the larger overall scattering cross sections. The former results in the underestimation of absorption, since some photons are forward-scattered into the detector. In contrast, an increase in scattering cross sections accounts for an overall loss of photons from the system, leading to an overestimation of absorption. For the 2 cm^3/sec flames described here, the smallest possible pupil that can be used corresponds to a collected angle of 0.086 degrees. For smaller angles, refracted light rays are intercepted by the pupil, resulting in gray-scale schlieren imaging. The requirement placed on input beam divergence to validate inversion by Abel transformation implies that for a pupil diameter of less than $(d_p \cdot f)/(M \cdot d_f)$, a collimated source is not required. For the present system, this value corresponds to a collection angle of 0.5 degrees. Providing that suitable source radiance is available to overcome natural flame emissions, imaging absorption experiments could, in principle, be performed using diffuse illumination, eliminating coherent effects and providing additional cost savings. This presumes that the source spectrum and spectrally-dependent refractive index of soot particles can be suitably characterized.

Conclusion

A technique has been developed for rapid acquisition of full-field optical extinction data. For flames possessing suitable geometries, this data can be tomographically inverted to provide two dimensional soot volume fraction maps. Compared to previously reported sequential, point-wise methods, this technique provides a two-fold improvement in spatial resolution and affords an increase in temporal throughput on

the order of 7×10^7. This allows the study of transient phenomena and the investigation of spatial and temporal correlations.

The optical configuration is simple and inexpensive. While the present system provides the measurement of fractional absorbances as low as 4×10^{-3} for a spatial resolution of 483 x 512 elements at a temporal rate of 30 image fields per second, further improvements can be realized through the use of detector arrays possessing higher pixel densities and/or more rapid framing rates. Although the sensitivity of the instrument is improved by corrupting the coherence of the source, these results indicate that the achievable threshold sensitivity will ultimately be limited by second-order refractive and coherent optical effects.

Since coherent optical effects represent an additive noise mechanism not typically encountered in single-point measurements, spatial smoothing has been applied to the resulting full-field data. Numerically simulated optical projection data confirms the ability to retrieve absorbance and soot volume fraction maps in this fashion. The validity of imaging volume fraction measurements has been confirmed both by direct comparison of point-wise and imaging data, and by the ability to reproduce previously reported soot volume fractions in laminar ethylene diffusion flames.

The ability to perform temporally resolved measurements has been exploited to investigate the previously unreported affect of temporal averaging. The lack of systematic convergence in the observed soot volume fractions leads to the conclusion that, in this application, time-averaging does not necessarily provide more meaningful data, but rather that low-Reynolds-number diffusion flames are extremely sensitive to perturbation by their surroundings. Reasonable agreement between spatially-smoothed, single-shot and temporally-averaged measurements leads to the further conclusion that the former can be interpreted as being representative, on average, of the actual soot volume fractions.

REFERENCES

1. Haynes, B. S., and Wagner, H. G., *Progress in Energy and Combustion Science*, 7:229-273 (1981).

2. T'ien, C. L., and Lee, S. C., *Progress in Energy and Combustion Science*, 8:41-59 (1982).

3. Santoro, R. J., Semerjian, H. G., and Dobbins, R. A., *Combustion and Flame*, 51:203-218 (1983).

4. Gore, J. P., and Faeth, G. M., *Twenty-First Symposium (International) on Combustion*, The Combustion Institute, 1986, p. 1521-1531.

5. Siegel, R., and Howell, J. R., *Thermal Radiation and Heat Transfer*, 2nd edition, McGraw-Hill, New York, 1981, p. 450-595.

6. Dalzell, W. H., and Sarofim, A. F., *Journal of Heat Transfer*, 91:100-104 (1969).

7. Chippett, S., and Gray, W.H., *Combustion and Flame*, 31:149-159 (1978).

8. Vaglieco, B. M., Baretta, F., and D'Alessio, A., *Combustion and Flame*, 79:259-271 (1990).

9. Dobbins, R. A., and Megaridis, C. M., *Langmuir*, 3:254-259 (1987).

10. Puri, R., Richardson, T. F., Santoro, R. J., and Dobbins, R. A., *Combustion and Flame*, 92:320-333 (1993).

11. Köylü, Ü. Ö., and Faeth, G. M., *Combustion and Flame*, 89:140-156 (1992).

12. Berry, M. V., and Percival, I. C., *Opt. Acta*, 33:577-591 (1986).

13. Mountain, R. D., and Mulholland, G. W., *Langmuir*, 4:1321-1326 (1988).

14. Ku, J. C., and Shin, K. H., *Journal of Heat Transfer*, 113:953-958 (1991).

15. Dobbins, D. A., and Megaridis, C. M., *Applied Optics*, 30:4747-4754 (1991).

16. Köylü, Ü. Ö., and Faeth, G. M., *Journal of Heat Transfer*, 115:409-417 (1993).

17. Abel, N. H., *J. Reiner Angew. Math.*, 1:153-157 (1826).

18. Dasch, C. J., *Applied Optics*, Vol. 31, No. 8:1146-1152 (1992).

19. Ramachandran, G. N., and Lakshminarayanan, A. V., *Proceedings of the National Academy of Sciences*, 68:2236-2240 (1971).

20. Shepp, L. A., and Logan, B. F., *IEEE Trans. Nucl. Sci.*, NS-21:228-236 (1974).

21. Santoro, R. J., Semerjian, H. G., Emmerman, P. J., and Goulard, R., *International Journal of Heat and Mass Transfer*, Vol. 24, No. 7:1139-1150 (1981).

22. Hughey, B. J., and Santavicca, D. A., *Combustion Science and Technology*, Vol. 29:167-190 (1982).

23. Hall, R. J., and Bonczyk, P. A., *Applied Optics*, Vol. 29, No. 31:4590-4598 (1990).

24. Dändliker, R., *Progress in Optics*, Vol. XVII, New Holland, New York, 1980, pps. 9-11.

25. Akima, H., *ACM Transactions on Mathematical Software*, 4:148-159 (1978).

26. Smith, W. J., *Modern Optical Engineering*, 2nd Edition, McGraw-Hill, New York, 1990, pps. 133-158.

27. Howes, W. L., and Buchele, D. R., *Journal of the Optical Society of America*, Vol. 56, No. 11:1517-1528 (1966).

28. Faeth, G. M., *Science Requirements Document for the Laminar Soot Processes Experiment (LSP)*, Submitted to the National Aeronautics and Space Administration, Code UG, 1994, pps. D.1-D.12.

Figure Captions

Fig. 1 Optical configuration for soot volume fraction imaging measurements.

Fig. 2 Unattenuated reference image with no diffuser present.

Fig. 3 Unattenuated reference image using rotating diffuser plate to corrupt coherence of the source.

Fig. 4 Absorbance map corresponding to the 3.85 cm^3/sec laminar ethylene diffusion flame.

Fig. 5 Soot volume fraction map corresponding to the 3.85 cm^3/sec laminar ethylene diffusion flame.

Fig. 6 Comparison of transmittance data with data of Santoro et al (ref. 3).

Fig. 7 Comparison of soot volume fractions with data of Santoro et al (ref. 3).

Fig. 8 Absorbance data for the 2 cm^3/sec laminar ethylene diffusion flame demonstrating the effect of temporal averaging.

Fig. 9 Absorbance data for the 2 cm^3/sec laminar ethylene diffusion flame; unsmoothed and smoothed profiles are shown for both single-shot and temporally averaged data sets.

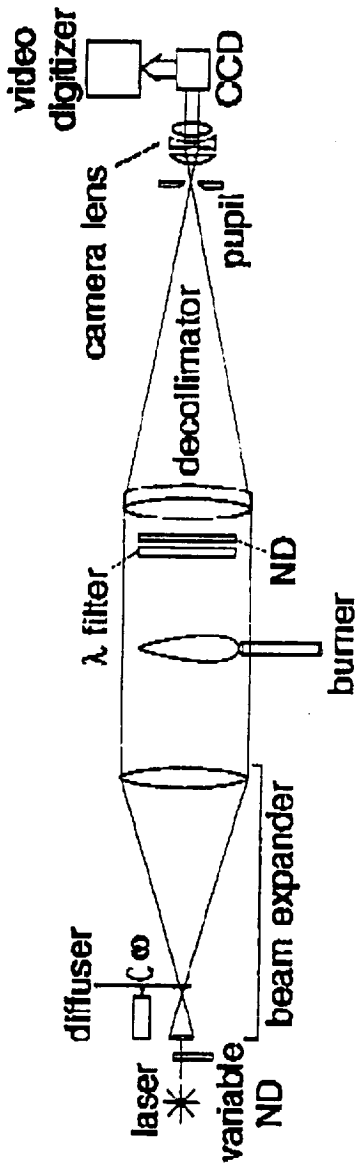
video digitizer
CCD
camera lens
pupil
decollimator
λ filter
ND
burner
beam expander
diffuser
laser
variable ND

Fig. 1

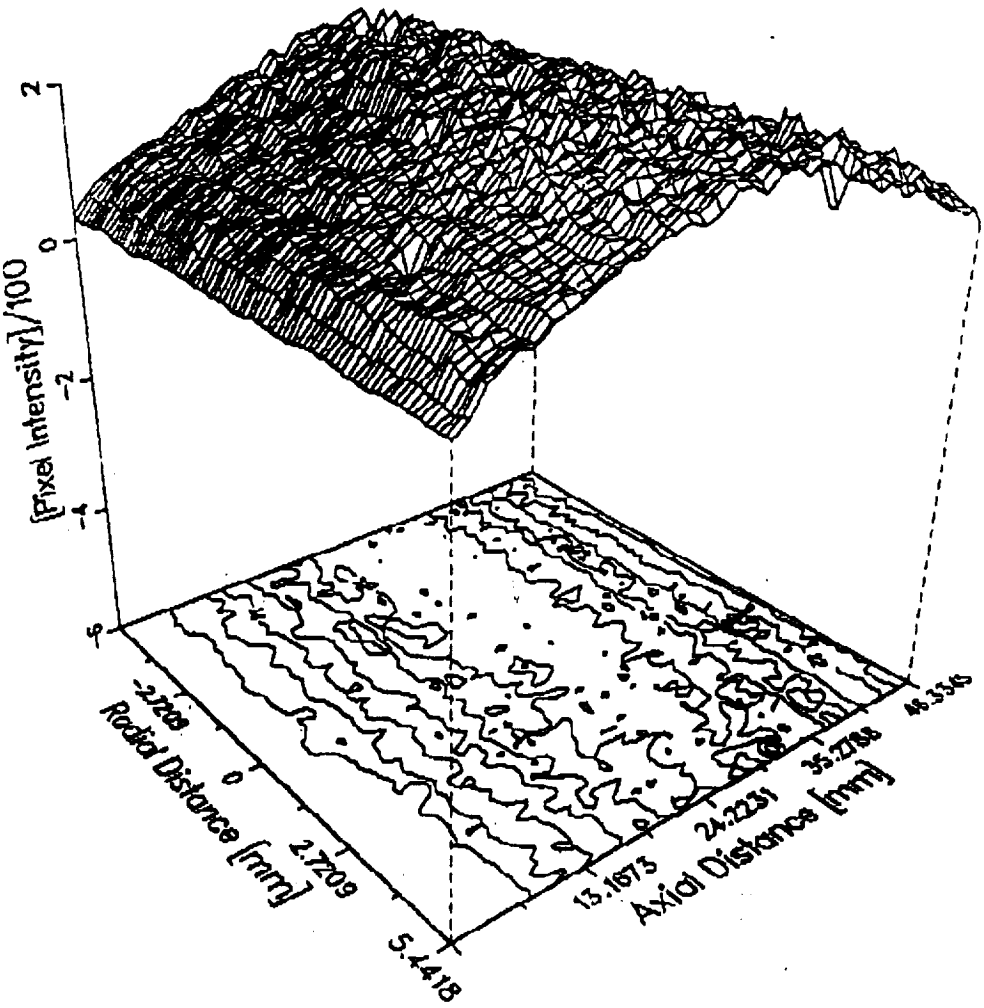
[Pixel Intensity]/100
2
0
-2
-4
-6
-2.709
0
2.709
5.418
Radial Distance [mm]
13.1673
24.2231
35.2788
46.3346
Axial Distance [mm]

Fig. 2

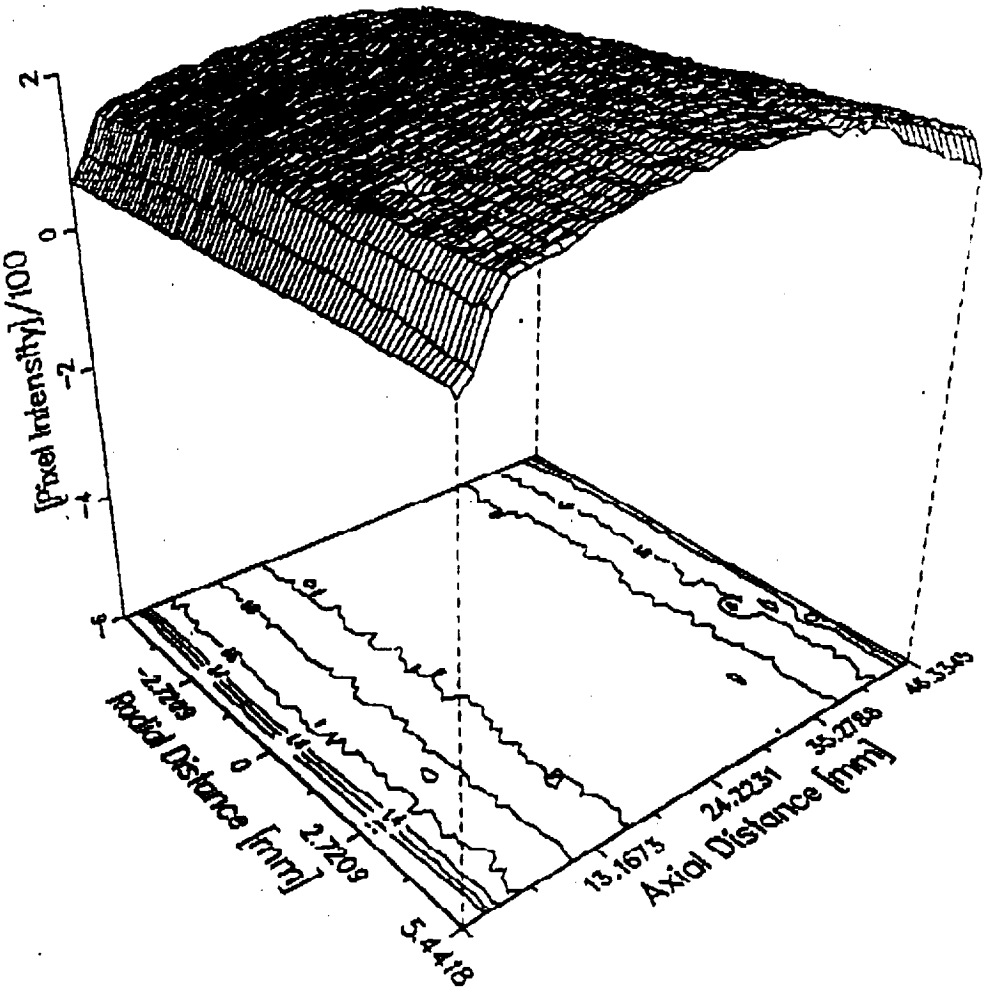
[Pixel Intensity]/100
2
0
-2
-4
-6
Radial Distance [mm]
-2.709
0
2.7209
5.4418
Axial Distance [mm]
13.1673
24.2231
35.2788
46.3345

Fig. 3

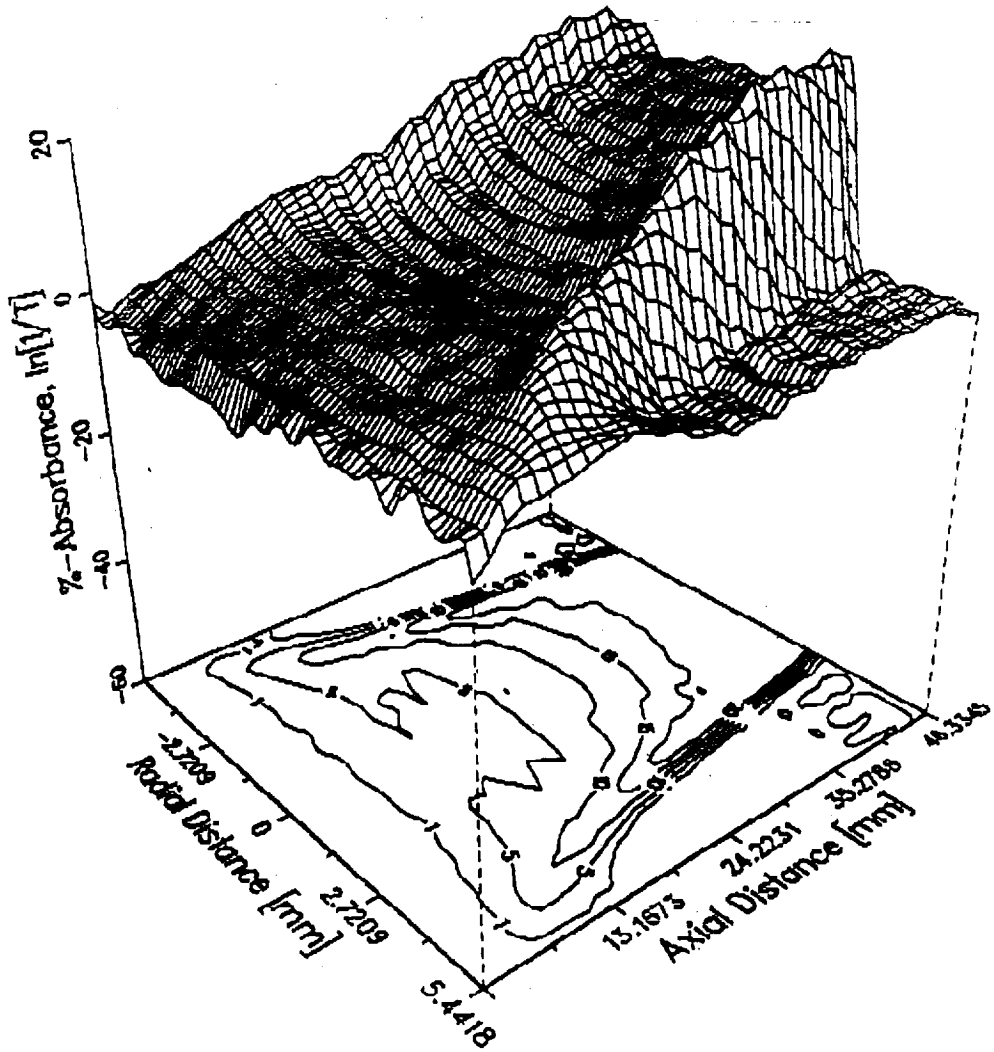
%-Absorbance, ln[I/I]
20
0
-20
-40
-60
-2.709
0
2.709
5.4418
Radial Distance [mm]
13.1673
24.2231
35.2788
46.3346
Axial Distance [mm]

Fig. 4

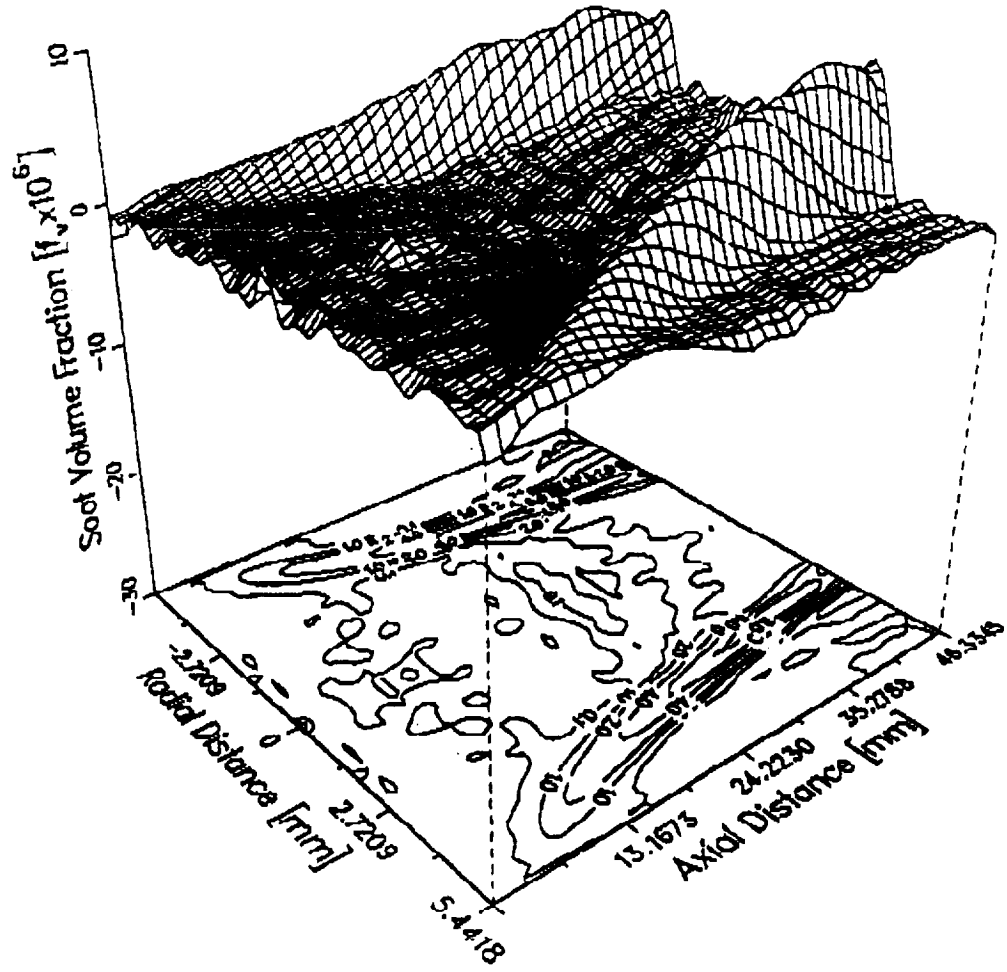
Soot Volume Fraction [f_v x10^6]
10
0
-10
-20
-30
Radial Distance [mm]
-2.709
0
2.709
5.4418
Axial Distance [mm]
13.1673
24.2230
35.2788
46.3345

Fig. 5

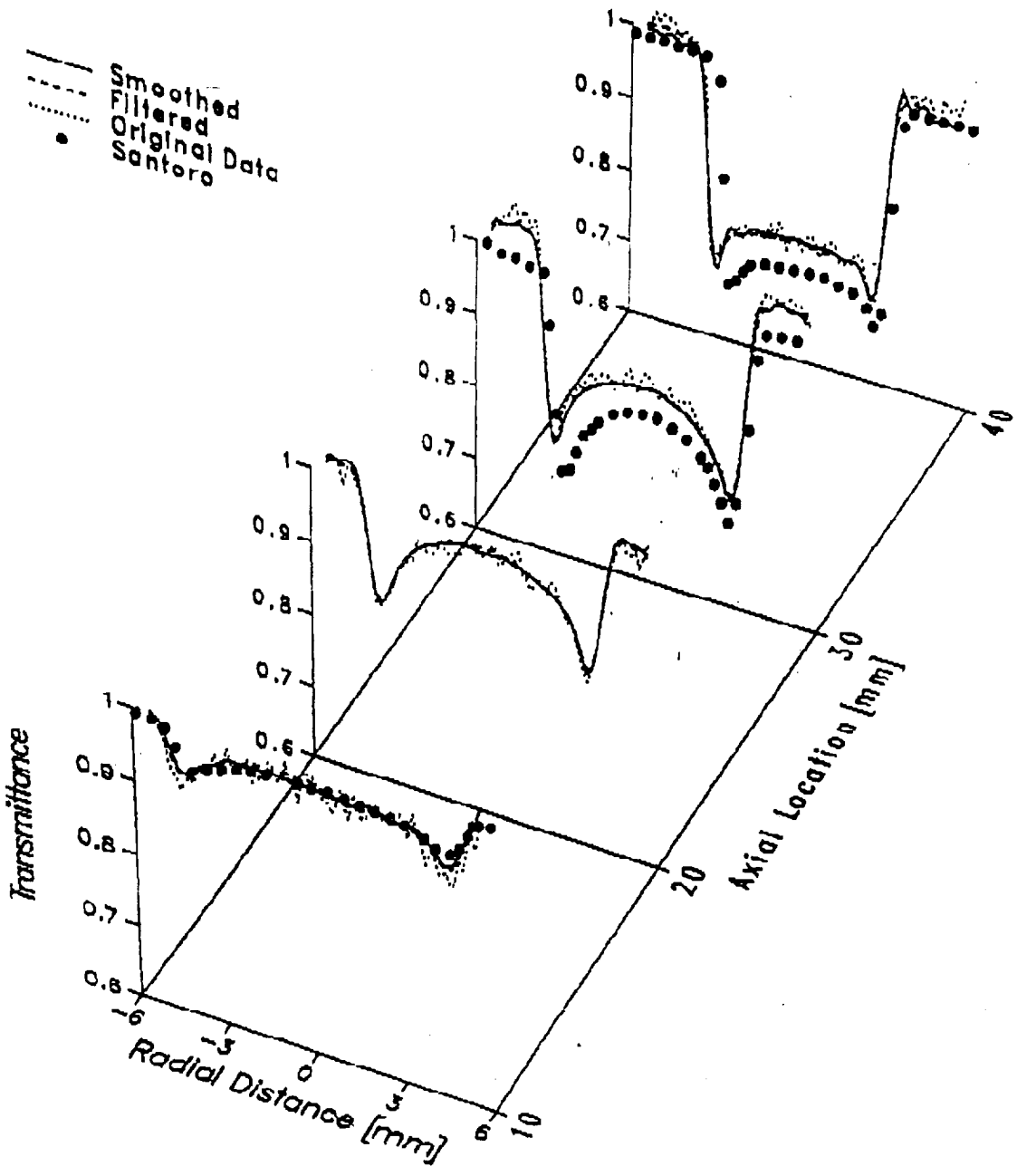
Smoothed
Filtered
Original Data
Santoro
Transmittance
Radial Distance [mm]
Axial Location [mm]

Fig. 6

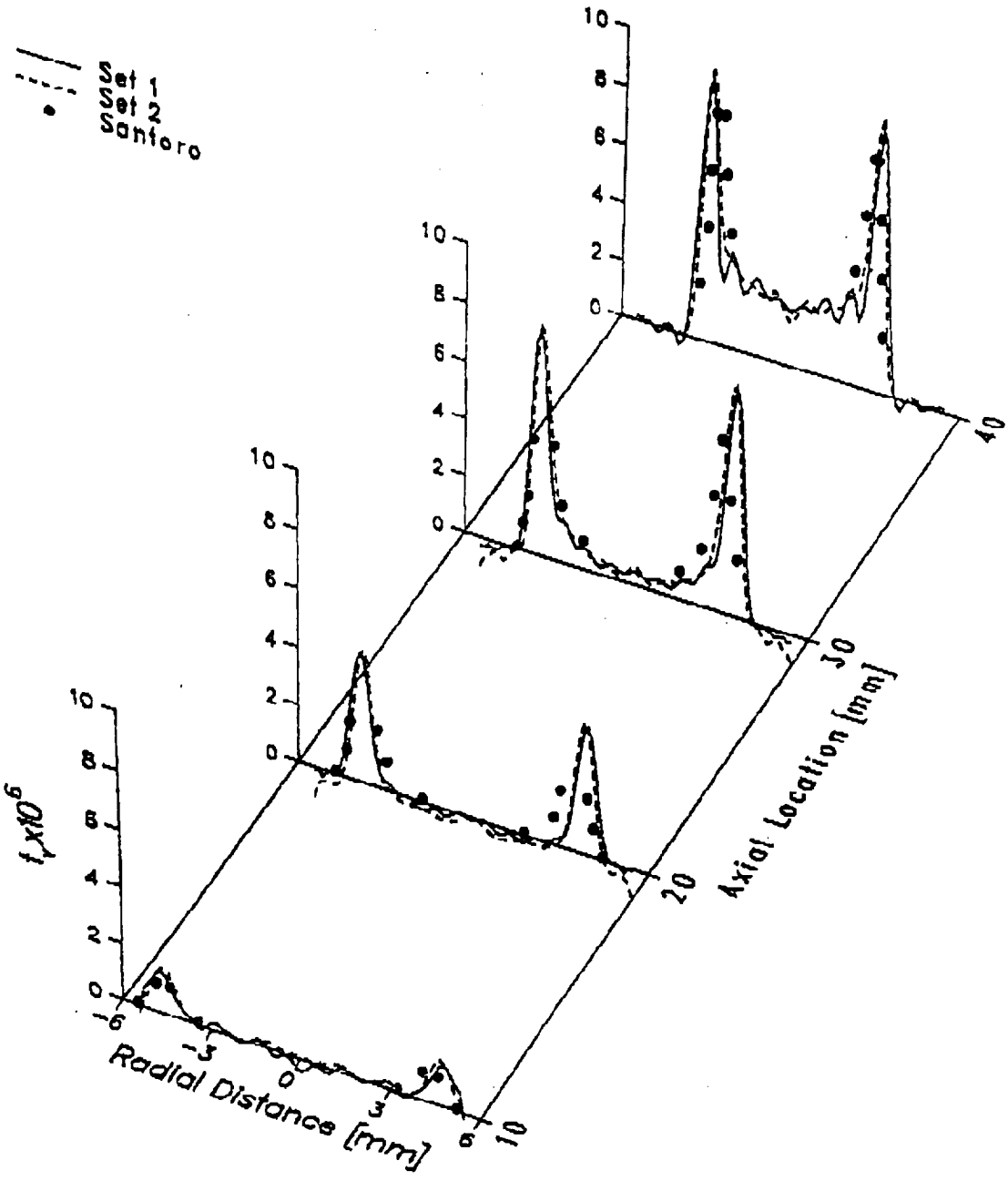
Set 1
Set 2
Santoro
$f_\phi \times 10^6$
Radial Distance [mm]
Axial Location [mm]

Fig. 7

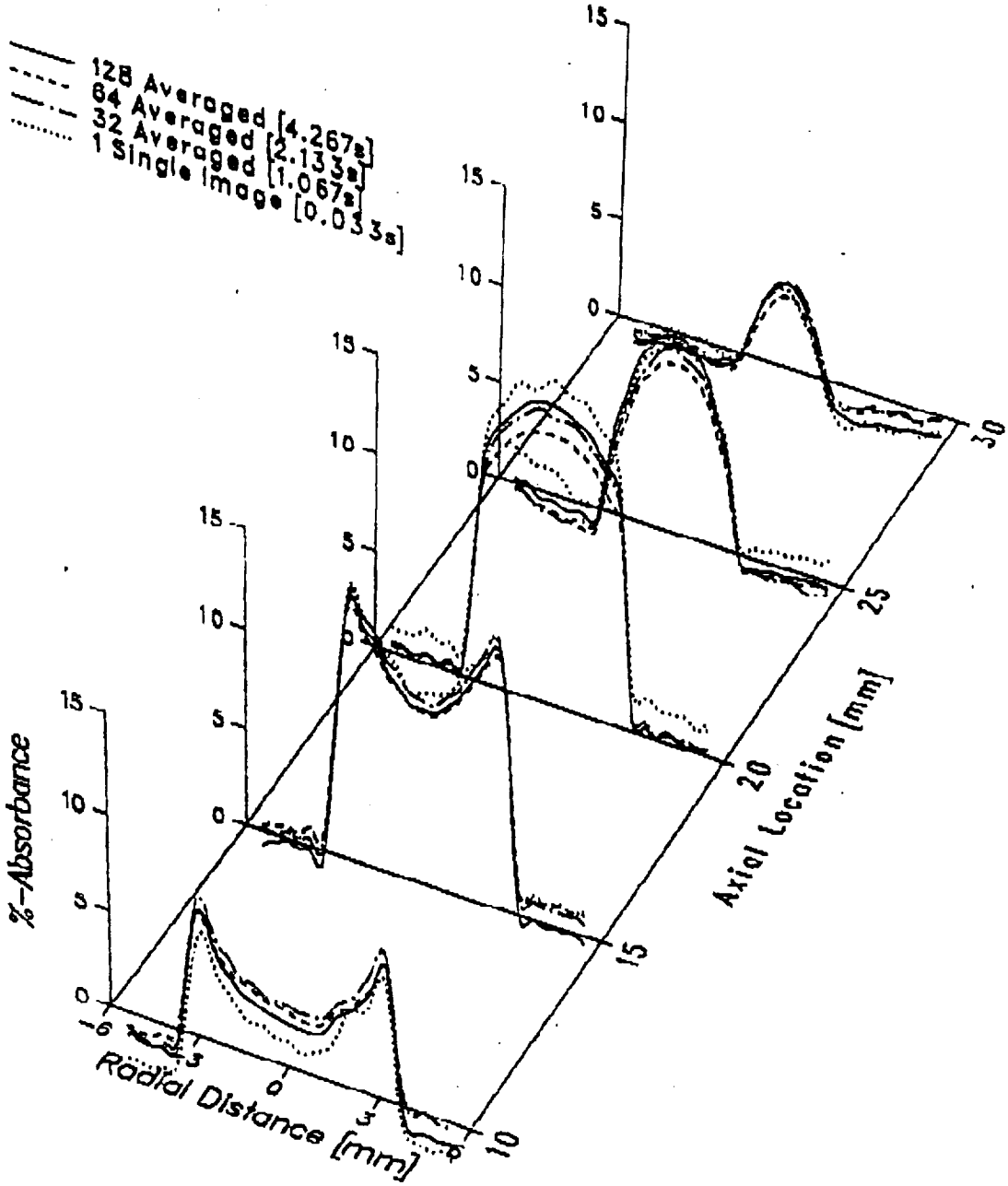
128 Averaged [4.267s]
64 Averaged [2.133s]
32 Averaged [1.067s]
1 Single Image [0.033s]
%-Absorbance
Radial Distance [mm]
Axial Location [mm]

Fig. 8

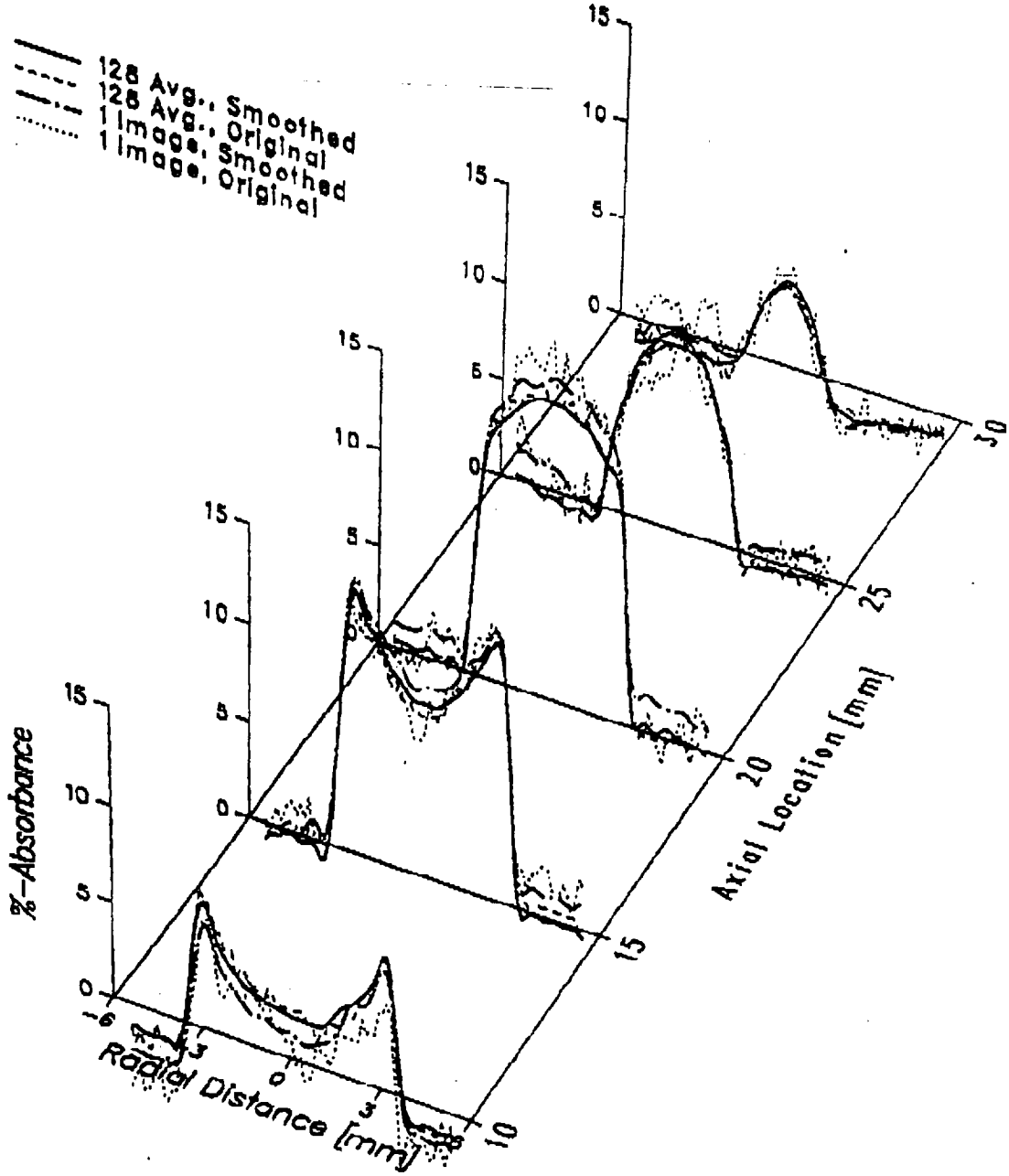
128 Avg., Smoothed
128 Avg., Original
1 Image, Smoothed
1 Image, Original
%-Absorbance
Radial Distance [mm]
Axial Location [mm]

Fig. 9